### **BIOMATERIALS**

## Soft strain-insensitive bioelectronics featuring brittle materials

Yichao Zhao<sup>1,2</sup>†, Bo Wang<sup>1</sup>†, Jiawei Tan<sup>1,2</sup>†, Hexing Yin<sup>2</sup>, Ruyi Huang<sup>3,4,5</sup>, Jialun Zhu<sup>1</sup>, Shuyu Lin<sup>1</sup>, Yan Zhou<sup>3,4</sup>, David Jelinek<sup>6,7</sup>, Zhengyang Sun<sup>6</sup>, Kareem Youssef<sup>2</sup>, Laurent Voisin<sup>6</sup>, Abraham Horrillo<sup>6</sup>, Kaiji Zhang<sup>1,2</sup>, Benjamin M. Wu<sup>2,8,9,10,11</sup>, Hilary A. Coller<sup>6,7,12</sup>, Daniel C. Lu<sup>3,4,5</sup>, Qibing Pei<sup>2</sup>, Sam Emaminejad<sup>1,10</sup>\*

<sup>1</sup>Interconnected and Integrated Bioelectronics Lab (I<sup>2</sup>BL), Department of Electrical and Computer Engineering, University of California, Los Angeles, CA, USA.

<sup>2</sup>Department of Materials Science and Engineering, University of California, Los Angeles, CA, USA.

<sup>3</sup>Department of Neurosurgery, David Geffen School of Medicine, University of California, Los Angeles, CA, USA.

<sup>4</sup>Neuromotor Recovery and Rehabilitation Center, David Geffen School of Medicine, University of California, Los Angeles, CA, USA.

15 <sup>5</sup>Brain Research Institute, University of California, Los Angeles, CA, USA.

<sup>6</sup>Department of Molecular, Cell and Developmental Biology, University of California, Los Angeles, CA, USA.

<sup>7</sup>Department of Biological Chemistry, David Geffen School of Medicine, University of California, Los Angeles, CA, USA.

<sup>8</sup>Weintraub Center for Reconstructive Biotechnology, School of Dentistry, University of California, Los Angeles, CA, USA.

<sup>9</sup>Division of Advanced Prosthodontics, School of Dentistry, University of California, Los Angeles, CA, USA.

<sup>10</sup>Department of Bioengineering, University of California, Los Angeles, CA, USA.

25 <sup>11</sup>Department of Orthopaedic Surgery, David Geffen School of Medicine, University of California, Los Angeles, CA, USA. \*Corresponding author. Email: emaminejad@ucla.edu

†These authors contributed equally to this work.

5

10

15

20

25

30

35

40

Advancing electronics to interact with tissue necessitates meeting material constraints in electrochemical, electrical, and mechanical domains simultaneously. Clinical bioelectrodes with established electrochemical functionalities are rigid and mechanically mismatched with tissue. Whereas conductive materials with tissue-like softness and stretchability are demonstrated, when applied to electrochemically probe tissue, their performance is distorted by strain and corrosion. We devise a layered architectural composite design that couples strain-induced cracked films with a strain-isolated out-of-plane conductive pathway and in-plane nanowire networks to eliminate strain effects on device electrochemical performance. Accordingly, we developed a library of stretchable, highly conductive, and strain-insensitive bioelectrodes featuring clinically established brittle interfacial materials (iridium-oxide, gold, platinum, and carbon). We paired these bioelectrodes with different electrochemical probing methods (amperometry, voltammetry, and potentiometry) and demonstrated strain-insensitive sensing of multiple biomarkers and in vivo neuromodulation.

Interfacing electronics with biological tissues is the foundation of probing and actuating biological systems. Reliable interaction between biological tissues and electronics requires the use of materials that support underlying electrochemical and electrical processes and satisfy tissue-imposed mechanical constraints (I, 2). The electrochemical process involves electron transfer and accumulation at the bioelectronics-tissue interface for in situ stimulation (for example, neuromodulation) and sensing (for example, biomarker molecules), necessitating the use of suitable interfacial materials. The electrical process involves electron transport for signal routing and setting intended operating points (for example, voltage), which requires the use of highly conductive materials (3). From the mechanics standpoint, materials that mimic tissue properties such as stretchability ( $\sim$ 20 to 75%) and compliance (Young's modulus, E, on the order of kilopascals – megapascals) are needed to establish conformable contact with tissue for high fidelity sensing and stimulation. This requirement is critical for minimizing disruption of tissue function as well as the risk of implant complications that result from scar formation, lead fracture, and tissue injury (I). However, the electrochemical and electrical performance of these materials may be affected by the strain originating from the movement and complex topography of the tissue.

Clinically established interfacial materials with high electrochemical performance for bioelectronics-tissue interfaces (such as noble metal-based ones) are all rigid (E > 1 GPa) and brittle (fracture strain < 1%). Recent advances in soft and stretchable conductors have enabled the development of strain-resilient devices with tissue-like mechanical properties, which maintain their electrical connection despite being extensively stretched (~800%) (4, 5). Although these strain-resilient devices are suitable for the construction and integration of soft, stretchable, solid-state electronics, when they are applied to electrochemically probe the tissue environment (involving ionic biofluid surrounding), their performance is distorted by strain- or corrosion-related issues. The former issue manifests in devices with relatively low intrinsic conductivity (such as graphene and PEDOT:PSS: 1 to  $10^3$  S/m), in which strain-induced changes to their resistance cause substantial deviation from the intended operating points (such as, activation voltage), subsequently corrupting the reactions at the interface (6-8). The latter issue is especially

<sup>&</sup>lt;sup>12</sup>Molecular Biology Institute, University of California, Los Angeles, CA, USA.

observed in devices with highly conductive materials that rapidly oxidize upon exposure to the surrounding solution (such as, silver-based nanomaterials), despite the application of surface modification [prone to surface defects or pores (9)]. As such, this group of devices cannot sustain the wide voltage range required to perform electrochemical reactions (5, 10).

5

10

15

20

25

30

35

40

45

We devised a layered architectural composite design that centers on decoupling the bioelectronic materials configuration into an interfacial element for electron transfer and an interconnection element for electron transport. This design allows for the exploiting and coupling of surface channel cracks (within the brittle interfacial element) and anisotropic out-of-plane/in-plane electron conduction (within the interconnection element) to eliminate strain effects on device performance. The design further allows for a broad selection for the interfacial materials, including brittle noble metal—based materials. Following this approach, we created a functionally diverse library of thin ( $\sim$ 140  $\mu$ m), soft ( $\sim$ 10 MPa) (fig. S1), stretchable (>150%), highly conductive ( $\sim$ 1 ohm/sq) and strain-insensitive bioelectrodes (SIBs).

Our fabrication strategy (Fig. 1A) is based on (i) constructing the tissue interfacing element as a thin film with favorable electron transfer characteristics, (ii) constructing the interconnection element by using intrinsically stretchable and highly conductive silver nanowire (AgNW)—based traces, which are inlaid in the surface layer of a soft rubbery matrix [poly(urethane acrylate), PUA], and (iii) seamlessly integrating the two elements by means of a thin adhesive and anisotropically conductive film (ACF), which features isolated conductive particles embedded in a stretchable matrix to facilitate anisotropic out-of-plane electrical conduction. A variety of thin-film materials, including those that are brittle but have high electrochemical performance [gold (Au) platinum (Pt), and iridium oxide (IrOx)], can be built atop the ACF-AgNW-PUA layers through standard thin-film deposition techniques (Fig. 1B).

Fundamentally, our SIB's strain insensitivity is controlled by three layer-specific strain energy dissipation mechanisms (Fig. 1, C and D, and fig. S2): (i) crack channeling of brittle interfacial thin film, (ii) strain isolation of the out-of-plane conductive pathway in the ACF layer, and (iii) realignment of in-plane AgNW networks. Interfacial channel cracks are exploited as means of tensile strain energy release. Each cracked fragment experiences minimal strain, while remaining electrically connected to the system, preserving the overall active surface area of the SIB. As the electrical bridge between the cracked interfacial thin film and the AgNW-PUA layer, the ACF renders strain-insensitive out-of-plane electrical conduction, because the rigid conductive microparticles (approximately gigapascals) are strain-isolated by the surrounding soft matrix (approximately kilopascals). The AgNWs in the bottom layer form in-plane conductive percolation networks that are strongly anchored onto the soft PUA substrate by means of in situ cross-linking. This strong binding enables network realignment to release strain energy (11).

The strain sensitivity of the electrical and electrochemical performances of the SIBs is compared with those obtained by the state-of-the-art stretchable bioelectrodes (Fig. 1E, fig. S3, and table S1) (7, 8, 10, 12, 13). We applied our SIBs to perform high-fidelity sensing of multiple biomarkers and neurostimulation under strain. We validated the in vivo operation of our SIBs in the context of a neural circuit. Specifically, we interfaced the bioelectrodes, featuring a brittle IrOx layer, with the sciatic nerve and verified the modulation of the bidirectional and interconnecting central nervous system (CNS) and motor unit (within the neural circuit) through peripheral nerve stimulation (PNS).

To visualize and quantitatively characterize the SIBs' strain insensitivity, we correspondingly used an electrochemical deposition-based staining method, electrical impedance

spectroscopy (EIS), and cyclic voltammetry (CV). We characterized Au-deposited SIBs (Au-SIBs) as model test devices over a range of tensile strain conditions. The devised electrochemical staining method enables the spatial mapping of the electrical connection of the interfacial thin film. It uses a standard electrodeposition setup to deposit a conductive material (in this application, Pt) onto a test electrode under strain, in which only the electrode surface regions that remain electrically connected to the power source support electrodeposition (Fig. 2A). As a result, the electrochemically deposited regions ("stained" regions) of the test electrodes exhibit a substantial imaging contrast under scanning electron microscopy (SEM) as compared with the nondeposited regions (fig. S4). As illustrated in figure 2B, the cracked fragments of a representative Au-SIB were fully "stained," indicating the preservation of their conductivity under varying large strain levels, in contrast to that of a control Au-elastomer electrode.

5

10

15

20

25

30

35

40

45

We characterized the cracked fragments by means of SEM imaging and analyzed the results with the aid of a dedicated statistical model (supplementary text S1). The results indicate that >99% of the brittle interfacial layer's surface area remains connected (fig. S5). Our cyclic stretching studies also demonstrate that the Au-SIB's crack density does not increase, despite repeated stretching (>10,000 cycles at 20% strain) (fig. S6A), and that the device's low resistance is minimally impacted during dynamic stretching (~2 ohm variation) (fig. S6B and C).

EIS and CV characterization results indicate that the changes to the SIB system's underlying electrochemical and electrical components (modeled in Fig. 2C) are negligible under strain. The impedance spectrum of representative 100% strained SIBs exhibited statistically identical curves in impedance magnitude (1 Hz to 100 kHz), as compared with their unstrained states (Fig. 2D and fig. S7). The SIB's electrochemical impedance has minimal change after 1000 cycles of tension (fig. S8). Furthermore, the CV plots of the unstrained and strained SIBs exhibit nearly identical features across 20 to 100% strain (Fig. 2, E to G). Without strain accommodation, tissue-induced strain causes a substantial increase in the interconnect resistance to the point of open circuit, which corrupts the electrode's electrical and electrochemical characteristics that manifest as as shifting and distortion of the EIS and CV curves, respectively (fig. S9).

Compared with bare AgNW-PUA, Au-SIB is more electrochemically stable (fig. S10). The underlying AgNW-PUA layer of the SIB does not experience galvanic corrosion in the presence of cracking. This contrasts with the case of Au-deposited AgNW-PUA electrodes, which galvanically corrode because of the crack-induced exposure of the AgNWs (fig. S11). The SIB's corrosion resistance indicates the protective role of the hydrophobic ACF in the prevention of AgNW oxidation and the release of cytotoxic Ag ions (useful for prolonged and biocompatible in vivo operations).

A diverse library of interfacial materials beyond Au can be simply incorporated into the SIB structure with standard thin film deposition techniques and paired with different application-specific electrochemical probing methods that involve wide ranging voltage and frequency conditions (Fig. 3A). We deposited Pt, carbon, and IrOx onto ACF as examples of commonly used brittle interfacial materials, leading to a series of SIBs with strain-insensitive interfacial electrochemical reaction features (validated with CV characterization) Fig. 3B). We applied these electrodes (exhibiting minimal device-to-device variation) (fig. S12) under large strain to carry out amperometry, voltammetry, and potentiometry, representing distinct electron transfer processes [Fig. 3, C (i, ii), D (i, ii), and E (i, ii)].

The choice of Pt as an interfacial material was motivated by its common use as a hydrogen peroxide (H<sub>2</sub>O<sub>2</sub>)-sensing layer in oxidase-based enzymatic biosensors. As shown in Fig. 3C, and

figs. S13A and S14A, the corresponding amperometric responses of the Pt-SIB at its relaxed and tensile states were similar for different concentrations of H<sub>2</sub>O<sub>2</sub>. These results indicate that the faradaic current was minimally affected by the strain despite the occurrence of the cracks. We also observed strain-insensitive H<sub>2</sub>O<sub>2</sub>-sensing when using Au as an interfacial material (fig. S15).

5

10

15

20

25

30

35

40

45

The choice of carbon as an interfacial material was motivated by its common use in the quantification of low-concentration electroactive biomarkers. We investigated the effect of strain on the response of the carbon-SIB electrodes in the context of differential pulse voltammetry (DPV) for the detection of acetaminophen. As shown in Fig. 3D (iii) and fig. S13B, the corresponding DPV peak current measured by the electrode at its relaxed versus tensile states were similar for different concentrations of acetaminophen. The strain-induced shift in redox potential was minimal (~0.1 V).

The choice of IrOx as an interfacial material was motivated by its substantial yet unrealized full potential in bioelectronics. IrOx is not only biocompatible but also facilitates fast and reversible redox reactions with surrounding hydrogen ions (14), enabling large and reversible current injection. The latter point in particular supports IrOx's superiority over noble metals such as Au and Pt for tissue bioelectronics applications such as pH sensing and neural stimulation. However, because of its intrinsic brittleness, IrOx cannot be easily engineered as an inherently stretchable electrode. Our fabrication strategy enabled simple engineering of IrOx-SIBs where the tight bonding of the IrOx film (supporting electron transfer) to the underlying layer (supporting electron transport) ensured robust device operation despite IrOx's brittleness. The fabricated IrOx-SIB possesses a charge storage capacity of ~12 mC/cm² (fig. S16), which is similar to the charge storage capacity of standard clinical stimulation electrodes (15).

We investigated the IrOx-SIB for potentiometric pH sensing [Fig. 3E(ii)] and AC excitation in the form of biphasic pulses, for neurostimulation [Fig. 3E(iv)]. The open-circuit potential measurements indicate that the IrOx-SIB responses are correlated with the tested solution's pH levels, and that the electrode responses remain unperturbed under both static and dynamic tensile states (Fig. 3E[iii] and fig. S13C and fig. S14B). As plotted in Fig. 3E (v) and fig. S17, the EIS measurements performed with our unstrained versus 40% strained IrOx-SIBs were similar, illustrating its strain insensitivity over a wide frequency range and informing its utility for both low- and high-frequency stimulation settings such as neuromodulation. Our studies in ex vivo neurostimulation characterization demonstrate the SIB's robustness in delivering stable current under both static and dynamic tensile conditions [Fig. 3E(vi) and fig. S14C].

As summarized in Fig. 4A, the IrOX-SIB presents electrochemical and electrical properties nearly identical to those of clinically used rigid cuff electrodes, while exhibiting tissue-like mechanical properties. The neural tissue-like mechanical characteristic of IrOx-SIB is advantageous over existing implantable electrodes that use rigid materials for neuromodulation because it potentially minimizes scar formation and immune response while rendering efficient stimulation even under deformation (1). To evaluate the performance of IrOx-SIBs during in vivo stimulation, we interfaced these bioelectrodes with the sciatic nerve to modulate the bidirectional and interconnecting spinal cord and muscles within the neural circuit (Fig. 4B). Accordingly, after validating its biocompatibility through cellular viability studies (fig. S18), the IrOx-SIB was applied in living mouse studies to deliver clinically relevant voltage and frequency stimulation conditions.

We concurrently recorded the real-time electromyography (EMG) of the bilateral anterior tibialis (TA) and medial gastral (MG) muscles innervated by the sciatic nerve (Fig. 4C). To

validate CNS neuromodulation, the subsequently expressed c-Fos protein levels (induced through sciatic nerve stimulation) in the lumbar spinal cord were labeled with immunofluorescent staining (Fig. 4C). Sciatic nerve stimulation with increasing voltage levels (at 1 Hz of frequency) led to the increase and following saturation of the TA and MG EMG intensities (Fig. 4, D and E). This trend indicates an increase in the synchronized recruitment of the available motor units, up to the point of full recruitment, which is achieved at potential levels as low as ~20 mV, thus illustrating efficient recruitment (8). As shown in Fig. 4, F and G, our studies involving sciatic nerve stimulation with excitation frequencies spanning from 1 to 100 Hz (at 100 mV) revealed the low-pass filtering characteristic (with cut-off frequency at ~20 Hz) of the muscle contraction (16). Despite being strained, our device induced TA and MG EMG with similar levels of signal-to-noise ratio (SNR; ~30 dB) as those produced by conventional electrodes (~10 to 38 dB at ~1 Hz) in unstrained settings (17, 18).

As shown in figure 4H, there is a one-to-one ratio between the applied stimulation frequencies and the recorded TA and MG muscle contraction frequencies. These results demonstrate the fidelity of the neural stimulation and the robustness of the strained SIB in supporting undistorted electron transfer and transport processes. From the standpoint of CNS neuromodulation (Fig. 4I), the c-Fos proteins are observably expressed in response to the sciatic nerve stimulation (Fig. 4K) (nonstimulated control shown in Fig. 4J). Furthermore, our staining results indicate the spatial concentration of the c-Fos expression in the dorsal horn of the spinal cord, which is related to the neural processing of sensory information such as pain.

We harnessed the superior electrochemical stability of diverse interfacial materials and the electrical conductivity of silver nanowire without being restricted by their inherent limitations in stretchable bioelectronic settings (interfacial materials' crack onset strain and silver nanowire's electrochemical instability). These materials were combined through the use of a strain-insensitive and anisotropic ultra-conductive film. We simultaneously achieved strain insensitivity, high conductivity, and electrochemical stability with a diverse array of interfacial materials. On a broader level, by unlocking mechanical constraints, the design principle allows for combining materials in ways to harness their superior properties in different domains. This allows for the attainment of maximum achievable performance offered across constituent materials.

## 30 References and Notes

5

10

15

20

- 1. R. Feiner, T. Dvir, Tissue–electronics interfaces: From implantable devices to engineered tissues. *Nat. Rev. Mater.* **3**, 17076 (2018). doi:10.1038/natrevmats.2017.76
- 2. S. P. Lacour, G. Courtine, J. Guck, Materials and technologies for soft implantable neuroprostheses. *Nat. Rev. Mater.* 1, 16063 (2016). doi:10.1038/natrevmats.2016.63
- 35 3. H. Yuk, B. Lu, X. Zhao, Hydrogel bioelectronics. *Chem. Soc. Rev.* **48**, 1642–1667 (2019). doi:10.1039/C8CS00595H Medline
  - 4. Y. Wang, S. Gong, S. J. Wang, X. Yang, Y. Ling, L. W. Yap, D. Dong, G. P. Simon, W. Cheng, Standing Enokitake-like Nanowire Films for Highly Stretchable Elastronics. *ACS Nano* 12, 9742–9749 (2018). doi:10.1021/acsnano.8b05019 Medline
- 5. S. Choi, S. I. Han, D. Jung, H. J. Hwang, C. Lim, S. Bae, O. K. Park, C. M. Tschabrunn, M. Lee, S. Y. Bae, J. W. Yu, J. H. Ryu, S.-W. Lee, K. Park, P. M. Kang, W. B. Lee, R. Nezafat, T. Hyeon, D.-H. Kim, Highly conductive, stretchable and biocompatible Ag-Au coresheath nanowire composite for wearable and implantable bioelectronics. *Nat. Nanotechnol.* 13, 1048–1056 (2018). doi:10.1038/s41565-018-0226-8 Medline

- Q. Zhai, Y. Wang, S. Gong, Y. Ling, L. W. Yap, Y. Liu, J. Wang, G. P. Simon, W. Cheng, Vertical Gold Nanowires Stretchable Electrochemical Electrodes. *Anal. Chem.* 90, 13498– 13505 (2018). doi:10.1021/acs.analchem.8b03423 Medline
- 7. Y. Liu, J. Liu, S. Chen, T. Lei, Y. Kim, S. Niu, H. Wang, X. Wang, A. M. Foudeh, J. B.-H. Tok, Z. Bao, Soft and elastic hydrogel-based microelectronics for localized low-voltage neuromodulation. *Nat. Biomed. Eng.* **3**, 58–68 (2019). <a href="https://doi.org/10.1038/s41551-018-0335-6">doi:10.1038/s41551-018-0335-6</a> Medline

10

15

- 8. J. Zhang, X. Liu, W. Xu, W. Luo, M. Li, F. Chu, L. Xu, A. Cao, J. Guan, S. Tang, X. Duan, Stretchable Transparent Electrode Arrays for Simultaneous Electrical and Optical Interrogation of Neural Circuits in Vivo. *Nano Lett.* **18**, 2903–2911 (2018). doi:10.1021/acs.nanolett.8b00087 Medline
- 9. H. Lee, S. Hong, J. Lee, Y. D. Suh, J. Kwon, H. Moon, H. Kim, J. Yeo, S. H. Ko, Highly Stretchable and Transparent Supercapacitor by Ag-Au Core-Shell Nanowire Network with High Electrochemical Stability. *ACS Appl. Mater. Interfaces* **8**, 15449–15458 (2016). doi:10.1021/acsami.6b04364 Medline
- 10. F. Decataldo, T. Cramer, D. Martelli, I. Gualandi, W. S. Korim, S. T. Yao, M. Tessarolo, M. Murgia, E. Scavetta, R. Amici, B. Fraboni, Stretchable Low Impedance Electrodes for Bioelectronic Recording from Small Peripheral Nerves. *Sci. Rep.* **9**, 10598 (2019). doi:10.1038/s41598-019-46967-2 Medline
- 20 11. J. Liang, L. Li, X. Niu, Z. Yu, Q. Pei, Elastomeric polymer light-emitting devices and displays. *Nat. Photonics* 7, 817–824 (2013). <a href="https://doi.org/10.1038/nphoton.2013.242">doi:10.1038/nphoton.2013.242</a>
  - 12. J. Deng, H. Yuk, J. Wu, C. E. Varela, X. Chen, E. T. Roche, C. F. Guo, X. Zhao, Electrical bioadhesive interface for bioelectronics. *Nat. Mater.* **20**, 229–236 (2021). doi:10.1038/s41563-020-00814-2 Medline
- 13. I. R. Minev, P. Musienko, A. Hirsch, Q. Barraud, N. Wenger, E. M. Moraud, J. Gandar, M. Capogrosso, T. Milekovic, L. Asboth, R. F. Torres, N. Vachicouras, Q. Liu, N. Pavlova, S. Duis, A. Larmagnac, J. Vörös, S. Micera, Z. Suo, G. Courtine, S. P. Lacour, Electronic dura mater for long-term multimodal neural interfaces. *Science* 347, 159–163 (2015). doi:10.1126/science.1260318 Medline
- 30 14. C. Boehler, S. Carli, L. Fadiga, T. Stieglitz, M. Asplund, Tutorial: Guidelines for standardized performance tests for electrodes intended for neural interfaces and bioelectronics. *Nat. Protoc.* **15**, 3557–3578 (2020). <a href="https://doi.org/10.1038/s41596-020-0389-2">doi:10.1038/s41596-020-0389-2</a> <a href="https://doi.org/10.1038/s41596-020-0389-2">Medline</a>
  - 15. S. J. Wilks, S. M. Richardson-Burns, J. L. Hendricks, D. C. Martin, K. J. Otto, Poly(3,4-ethylenedioxythiophene) as a Micro-Neural Interface Material for Electrostimulation. *Front. Neuroeng.* **2**, 7 (2009). doi:10.3389/neuro.16.007.2009 Medline
    - 16. H. J. Freund, Motor unit and muscle activity in voluntary motor control. *Physiol. Rev.* **63**, 387–436 (1983). doi:10.1152/physrev.1983.63.2.387 Medline
- 17. S. Kim, L. K. Jang, M. Jang, S. Lee, J. G. Hardy, J. Y. Lee, Electrically Conductive Polydopamine-Polypyrrole as High Performance Biomaterials for Cell Stimulation in Vitro and Electrical Signal Recording in Vivo. *ACS Appl. Mater. Interfaces* **10**, 33032–33042 (2018). <a href="https://doi.org/10.1021/acsami.8b11546">doi:10.1021/acsami.8b11546</a> Medline
  - 18. P. Sabetian, "Improved Peripheral Nerve Recording with a Small Form-factor Nerve Electrode;

- A Novel Bipolar Nerve Cuff Design," University of Toronto, Toronto, ON (2015).
- 19. D. Jung, C. Lim, H. J. Shim, Y. Kim, C. Park, J. Jung, S. I. Han, S.-H. Sunwoo, K. W. Cho, G. D. Cha, D. C. Kim, J. H. Koo, J. H. Kim, T. Hyeon, D.-H. Kim, Highly conductive and elastic nanomembrane for skin electronics. *Science* 373, 1022–1026 (2021). doi:10.1126/science.abh4357 Medline

- 20. Y. J. Yun, J. Ju, J. H. Lee, S.-H. Moon, S.-J. Park, Y. H. Kim, W. G. Hong, D. H. Ha, H. Jang, G. H. Lee, H.-M. Chung, J. Choi, S. W. Nam, S.-H. Lee, Y. Jun, Highly Elastic Graphene-Based Electronics Toward Electronic Skin. *Adv. Funct. Mater.* 27, 1701513 (2017). doi:10.1002/adfm.201701513
- 21. N. Liu, A. Chortos, T. Lei, L. Jin, T. R. Kim, W.-G. Bae, C. Zhu, S. Wang, R. Pfattner, X. Chen, R. Sinclair, Z. Bao, Ultratransparent and stretchable graphene electrodes. *Sci. Adv.* 3, e1700159 (2017). doi:10.1126/sciadv.1700159 Medline
  - 22. Z. Yu, X. Niu, Z. Liu, Q. Pei, Intrinsically stretchable polymer light-emitting devices using carbon nanotube-polymer composite electrodes. *Adv. Mater.* **23**, 3989–3994 (2011). doi:10.1002/adma.201101986 Medline
  - 23. L. Cai, L. Song, P. Luan, Q. Zhang, N. Zhang, Q. Gao, D. Zhao, X. Zhang, M. Tu, F. Yang, W. Zhou, Q. Fan, J. Luo, W. Zhou, P. M. Ajayan, S. Xie, Super-stretchable, transparent carbon nanotube-based capacitive strain sensors for human motion detection. *Sci. Rep.* 3, 3048 (2013). doi:10.1038/srep03048 Medline
- 24. S. Lee, D. Sasaki, D. Kim, M. Mori, T. Yokota, H. Lee, S. Park, K. Fukuda, M. Sekino, K. Matsuura, T. Shimizu, T. Someya, Ultrasoft electronics to monitor dynamically pulsing cardiomyocytes. *Nat. Nanotechnol.* **14**, 156–160 (2019). <a href="mailto:doi:10.1038/s41565-018-0331-8">doi:10.1038/s41565-018-0331-8</a> <a href="mailto:Medline">Medline</a>
- 25. C. F. Guo, T. Sun, Q. Liu, Z. Suo, Z. Ren, Highly stretchable and transparent nanomesh electrodes made by grain boundary lithography. *Nat. Commun.* 5, 3121 (2014). doi:10.1038/ncomms4121 Medline
  - 26. F. Xu, Y. Zhu, Highly conductive and stretchable silver nanowire conductors. *Adv. Mater.* **24**, 5117–5122 (2012). doi:10.1002/adma.201201886 Medline
- 27. Y. Chen, R. S. Carmichael, T. B. Carmichael, Patterned, Flexible, and Stretchable Silver Nanowire/Polymer Composite Films as Transparent Conductive Electrodes. *ACS Appl. Mater. Interfaces* 11, 31210–31219 (2019). doi:10.1021/acsami.9b11149 Medline
  - 28. Y. Yu, S. Luo, L. Sun, Y. Wu, K. Jiang, Q. Li, J. Wang, S. Fan, Ultra-stretchable conductors based on buckled super-aligned carbon nanotube films. *Nanoscale* 7, 10178–10185 (2015). doi:10.1039/C5NR01383F Medline
- 29. Y. Wang, C. Zhu, R. Pfattner, H. Yan, L. Jin, S. Chen, F. Molina-Lopez, F. Lissel, J. Liu, N. I. Rabiah, Z. Chen, J. W. Chung, C. Linder, M. F. Toney, B. Murmann, Z. Bao, A highly stretchable, transparent, and conductive polymer. *Sci. Adv.* 3, e1602076 (2017). doi:10.1126/sciadv.1602076 Medline
- 30. H. He, L. Zhang, X. Guan, H. Cheng, X. Liu, S. Yu, J. Wei, J. Ouyang, Biocompatible Conductive Polymers with High Conductivity and High Stretchability. *ACS Appl. Mater. Interfaces* **11**, 26185–26193 (2019). doi:10.1021/acsami.9b07325 Medline

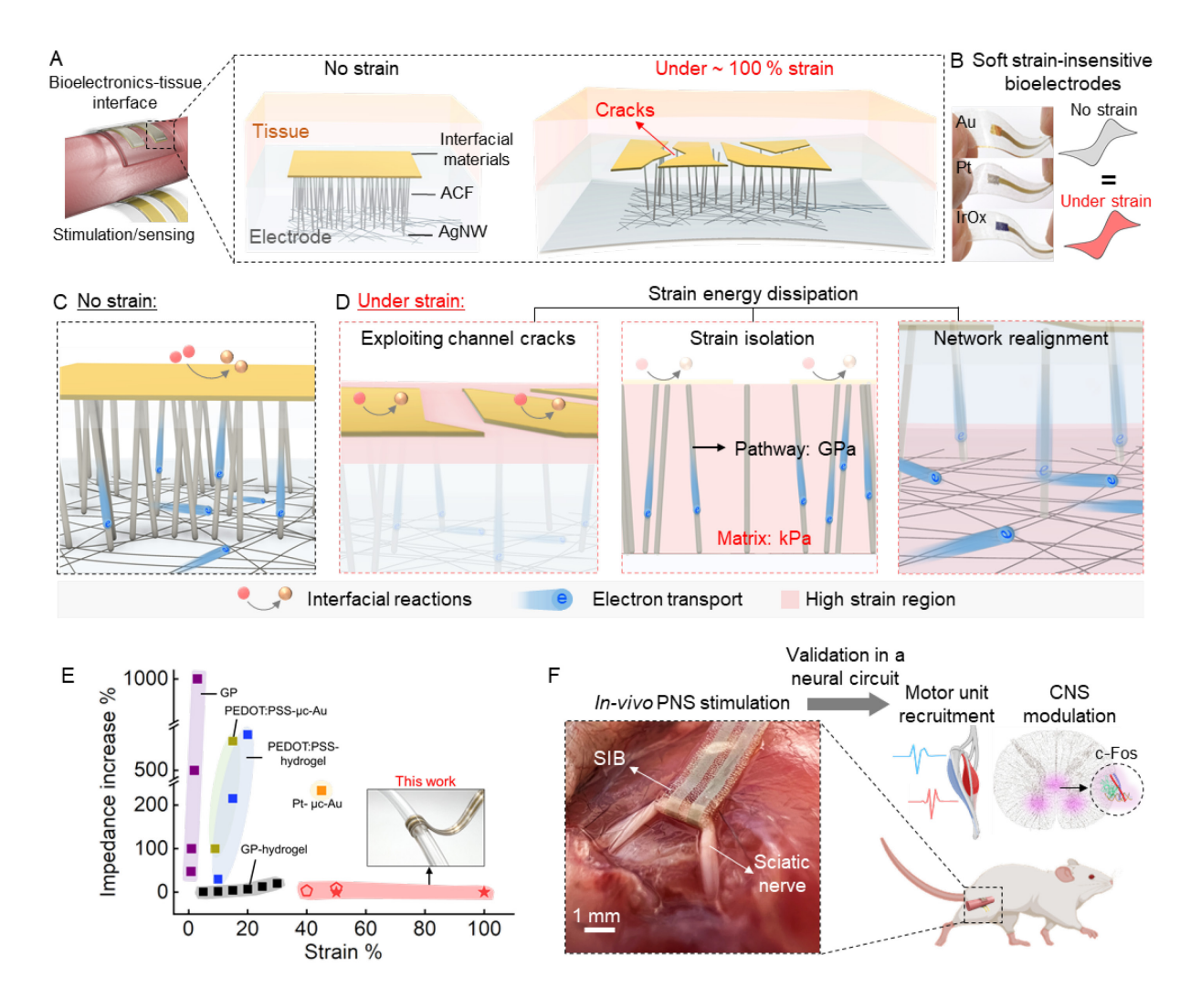


**Fig. 1. Soft strain-insensitive bioelectrode (SIB): architecture, strain dissipation mechanisms, and applications.** (A) Illustration of the SIB as a bioelectronics-tissue interface under strain. (B) Brittle noble metal—enabled SIBs for high fidelity stimulation and sensing under strain. (C) Schematic presentation of the SIB's underlying electron transfer and out-of-plane and in-plane electron transport processes. (D) Strain energy dissipation mechanisms within each layer of the SIB. (E) Ashby diagram of electrochemical impedance (at 1 kHz) increase versus tensile strain (7, 8, 10, 12, 13). Au-SIB and IrOx-SIB are indicated with star and pentagon markers, respectively. (F) A representative SIB interfacing the sciatic nerve of a mouse for nerve stimulation to achieve synchronized motor unit recruitment and CNS modulation, manifested as c-Fos expression.

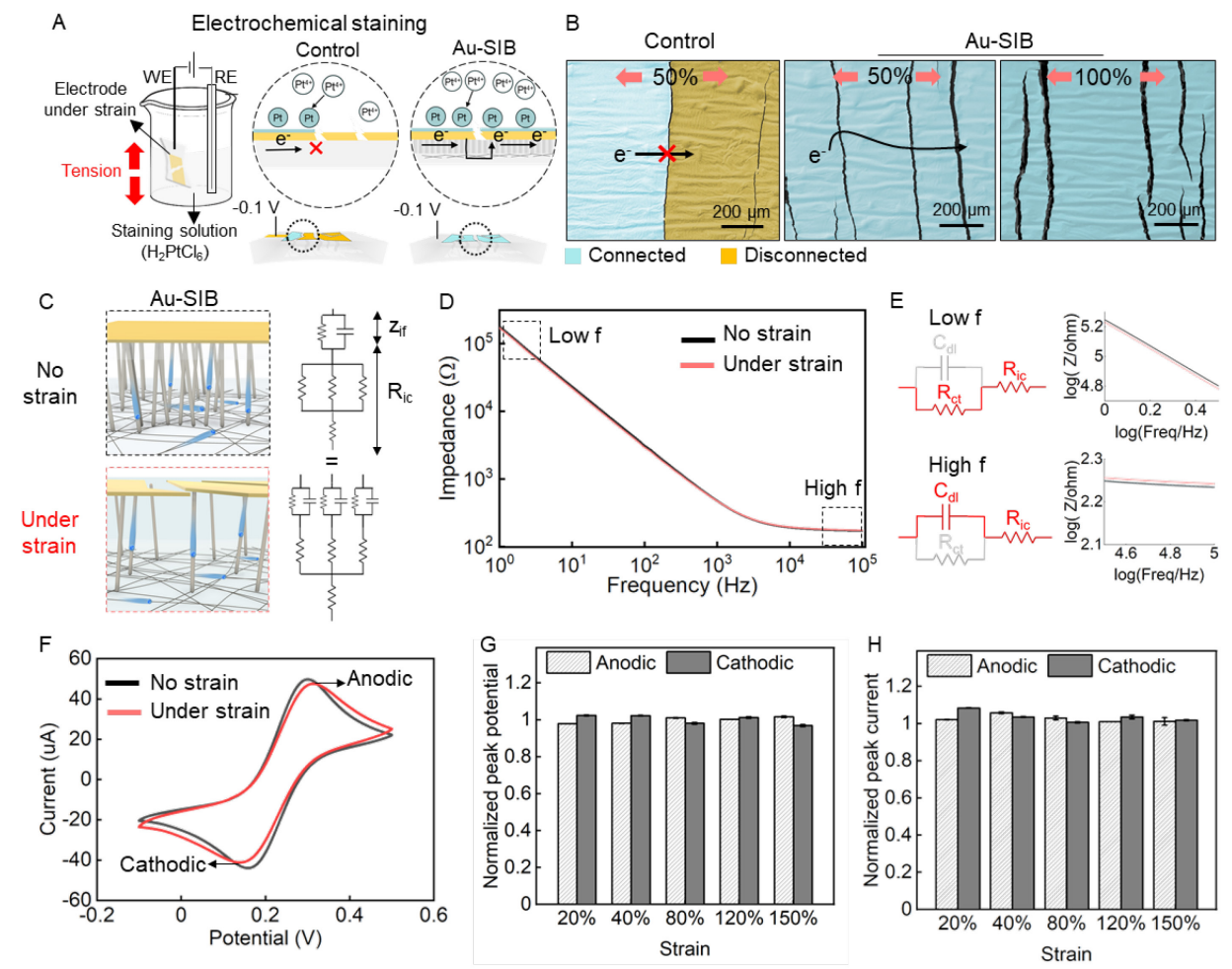
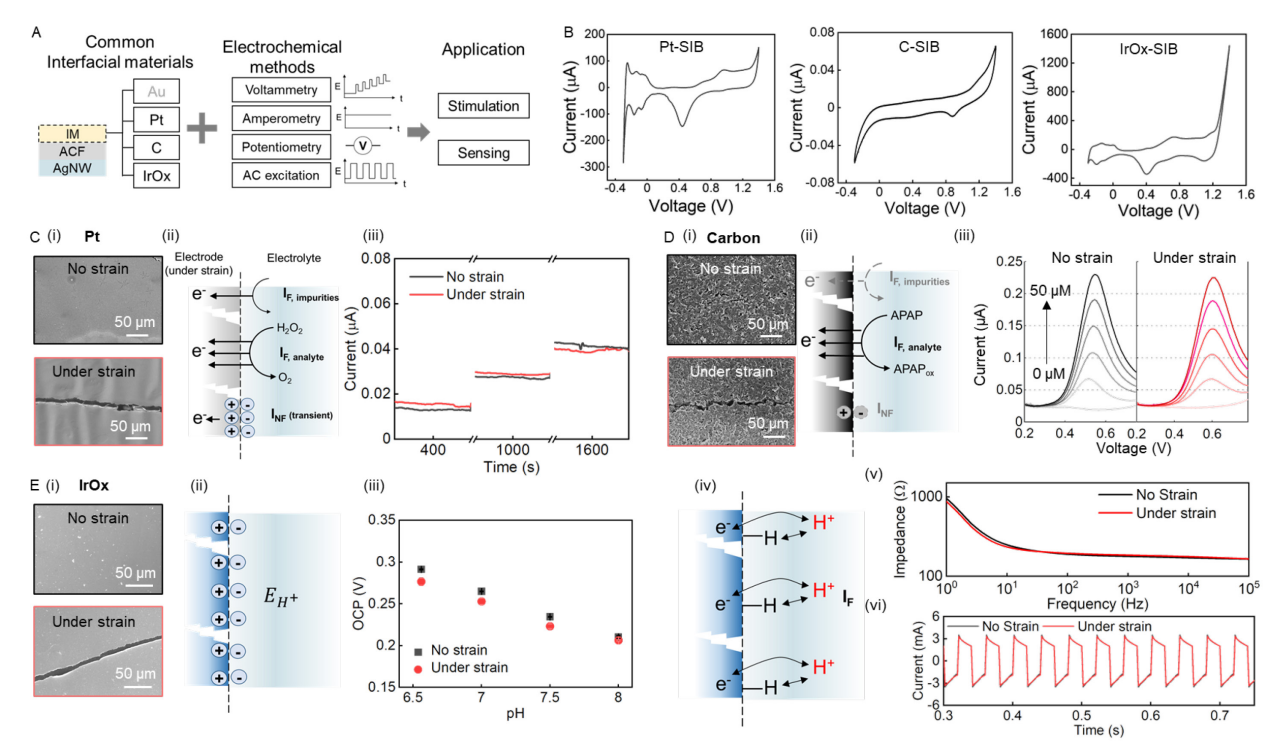


Fig. 2. Visualization and electrochemical characterization of Au-SIB performance under strain. (A) Schematic of the introduced electrochemical staining method. (B) Colored SEM images of the electrochemically stained control (Au, ACF, and PUA) electrode and Au-SIB under strain. They illustrate the electrical disconnection of a cracked fragment in the control electrode, whereas the Au-SIB's cracked fragments remained electrically connected. (C) Corresponding Randles model schematics of unstrained and strained or cracked SIBs. Interconnect resistance: Ric. Interfacial impedance: Zif. The SIB design enables the formation of parallel pathways for electron transfer and transport and maintenance of the active surface area under strain. (D) EIS comparison of Au-SIBs: unstrained versus 100% tensile-strained (n = 3 measurements by the same device for each strain condition). P = 0.12 comparing strained and unstrained measurement groups. Error bars indicate SEM. (E) CV comparison of Au-SIBs: unstrained versus 100% tensile-strained (in K<sub>3</sub>Fe(CN)<sub>6</sub> solution). (F and G) The anodic and cathodic peak positions (F) and heights (G) of Au-SIBs under 20% through 80% strain (normalized to unstrained values; N = 3; p values 0.053 to 0.745; error bars indicate SEM).

10



**Fig. 3.** A library of SIBs featuring brittle interfacial materials for electrochemical sensing and stimulation. (A) Pairing of SIBs with different electrochemical probing methods for diverse applications. IM represents the interfacial material layer. (**B**) CV characteristics of Pt-SIB, Carbon-SIB, and IrOx-SIB at 40% tensile strain versus unstrained state. (**C**) Pt-SIB characterization: (i) SEM images of the unstrained and 40% strained Pt-SIBs, (ii) schematic of the amperometric H<sub>2</sub>O<sub>2</sub> sensing process, and (iii) Pt-SIB's H<sub>2</sub>O<sub>2</sub> responses (0, 50, and 100 μM) at 40% tensile strain versus unstrained. (**D**) Carbon-SIB characterization: (i) SEM images of the unstrained and 100% strained carbon-SIBs, (ii) schematic of the DPV acetaminophen (APAP) sensing process, and (iii) carbon-SIB's APAP responses at 100% tensile strain versus unstrained. (**E**) IrOx-SIB characterization: (i) SEM images of the unstrained and 40% strained IrOx-SIBs, (ii) schematic of the pH sensing process, (iii) IrOx-SIB's pH open circuit potential (OCP) responses at 40% tensile strain versus Unstrained, (iv) schematic of the faradaic process for neurostimulation, and (v, vi) corresponding EIS and ex vivo neurostimulation characterization of the IrOx-SIBs at 40% tensile strain versus unstrained.

10

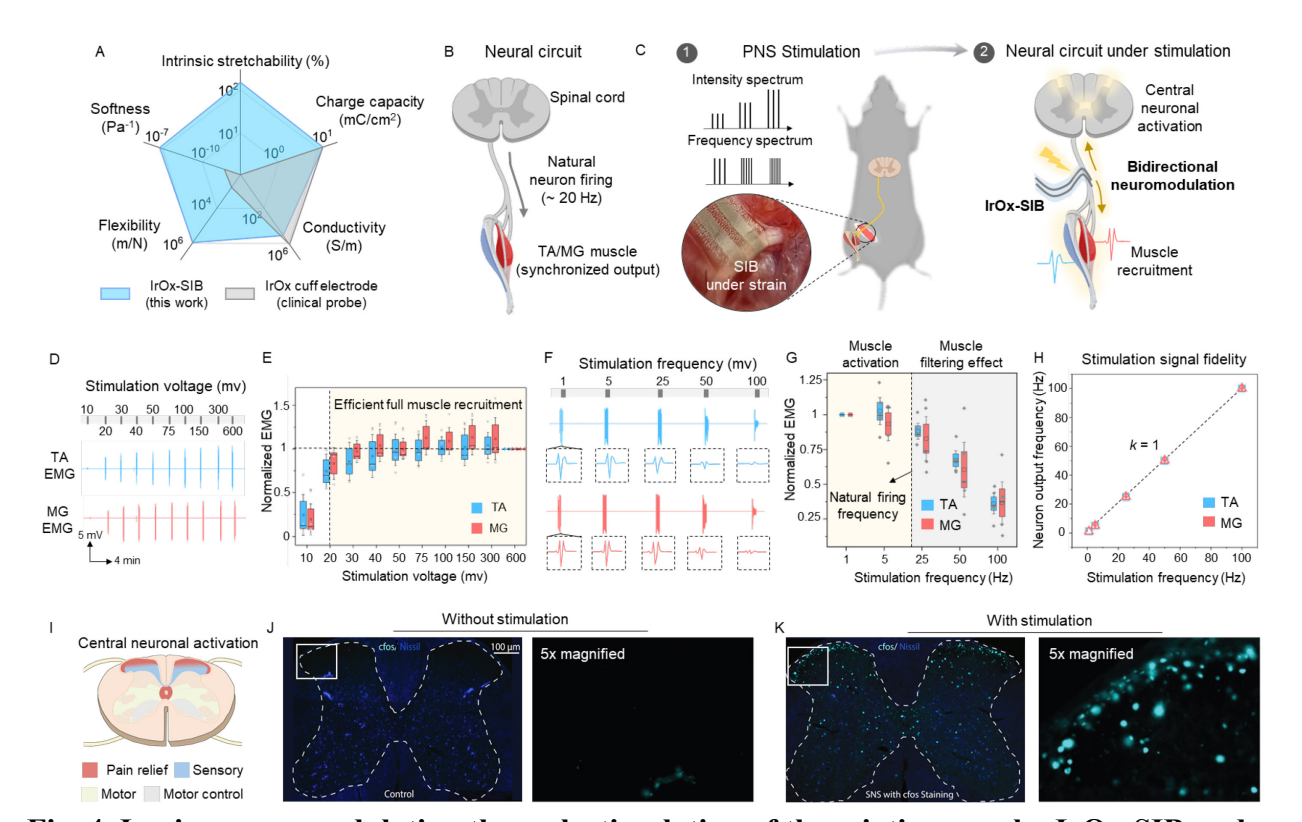


**Fig. 4.** In vivo neuromodulation through stimulation of the sciatic nerve by IrOx-SIB under deformation. (A) Radar chart of electrochemical, electrical, and mechanical properties of IrOx-SIB versus a standard IrOx cuff electrode. (B) Illustration of the neural circuit of a mouse. (C) In vivo evaluation of IrOx-SIB neuromodulation performance in an established neural circuit model. PNS responses were monitored through TA and MG recordings and CNS neuromodulation was evaluated through c-Fos staining of the lumbar spinal cord. (D to G) Sciatic nerve stimulation with different stimulation voltages at 1 Hz [(D) and (E)] and frequencies at 100 mV [(F) and (G)], and the correspondingly induced TA and MG muscle EMG recordings [(D) and (F)] and their respective normalized amplitudes [(E) and (G)]. (H) Comparison of the frequency of TA and MG neural signal outputs captured in G versus the stimulation frequency. (I) Schematics of regions determined by their neural functions within the spinal cord. (J and K) c-Fos expression patterns within lumbar spinal cord with (K) and without (J) sciatic nerve stimulation. Whole spinal cord staining (c-Fos single channel) images and zoomed-in views of the selected regions are shown. Dark blue color represents nissil staining and cyan color represents c-Fos staining.

# Acknowledgments

5

10

15

20

25

The authors appreciate the members of the UCLA nanoelectronics research facility (NRF) for their help in microfabrication/characterization. The authors extend their gratitude to L. Jin as well as to H. Lin, X. Cheng, H. Hojaiji and W. Yu for providing feedback on the presented work and insightful discussions. The authors also thank K. Sabet for statistical analysis; W. Yan for mechanical testing; and A. Vo, J. Park, and Y. Jinka for their assistance with device fabrication and BioRender.com. for figures creation. **Funding:** This work was supported by National Science Foundation (CAREER Award 1847729, S.E.); Startup package provided by the UCLA Henry Samueli School of Engineering and Applied Sciences (S.E.); National Institutes of Health (NIH) R21 DK128711-01 (S.E.); Innovation Award from the Broad Stem Cell Center (H.C.); NIH 1 R01 CA221296-01A1 (H.C.); NIH

1 R01 AR070245 (H.C.); DARPA HR0011-19-C-0043 (O.P.); UCLA ECE Departmental Fellowship (Y.Z.). Author contributions: Conceptualization: Y.Z., B.W., and S.E. Methodology: Y.Z., B.W., J.T., H.Y., R.H., B.M.W., H.C., D.L., Q.P., and S.E. Investigation: Y.Z., B.W., J.T., H.Y., R.H., J.Z., S.L., Y.Z., D.J., Z.S., K.Y., L.V., A.H., K.Z., H.C., D.L., Q.P., and S.E. Visualization: Y.Z., B.W., J.T., R.H., J.Z., and S.L. Funding acquisition: H.C., D.L., Q.P., and S.E. Project administration: Y.Z. and B.W. Supervision: H.C., D.L., Q.P., and S.E. Writing – original draft: Y.Z., B.W., J.T., R.H., H.C., Q.P., and S.E. Writing – review and editing: Y.Z., B.W., J.T., H.Y., R.H., H.C., Q.P., and S.E. Competing interests: S.E., Y.Z., B.W, Q.P., E.A., and Y.S. are applying for patents related to the described work. Data and materials availability: All data are available in the main text or the supplementary materials. License information: Copyright © 2022 the authors, some rights reserved; exclusive licensee American Association for the of Science. claim to government Advancement No original US https://www.science.org/about/science-licenses-journal-article-reuse

## 15 Supplementary Materials

science.org/doi/10.1126/science.abn5142

Materials and Methods

Supplementary Text

Figs. S1 to S18

20 Table S1

5

10

References 19-30

Submitted 31 December 2021; accepted 21 October 2022



# Supplementary Materials for

Enabling brittle materials for soft strain-insensitive bioelectronics

Yichao Zhao†, Bo Wang†, Jiawei Tan†, Hexing Yin, Ruyi Huang, Jialun Zhu, Shuyu Lin, Yan Zhou, David Jelinek, Zhengyang Sun, Kareem Youssef, Laurent Voisin, Abraham Horrillo, Kaiji Zhang, Benjamin M. Wu, Hilary A. Coller, Daniel C. Lu, Qibing Pei, Sam Emaminejad\*

Correspondence to: emaminejad@ucla.edu

## This PDF file includes:

Materials and Methods Supplementary Text Figs. S1 to S18 Table S1

#### **Materials and Methods**

## Preparation of Silver nanowire (AgNW)/poly (urethane acrylate) (PUA)

A dispersion of AgNWs in isopropanol (concentration: 2 mg/ml) was coated on glass substrates using a Meyer rod (RD Specialist) or airbrush (Paasche). The resulting conductive coating on the glass substrates was then coated with a precursor solution consisting of 100 weight parts urethane acrylate (UA, CN990), 20 parts ethylene butyl acrylate (EBA, SR540) and 1-part dimethylolpropionic acid (DMPA, Sigma-Aldrich). The coatings were cured on a Dymax ultraviolet curing conveyor equipped with a 2.5 W/cm² Fusion 300S type 'H' ultraviolet curing bulb, at a speed of 0.9 feet per minute for one pass, and then peeled off as a freestanding unit.

## Construction of strain-insensitive bioelectrodes (SIBs)

An anisotropic conductive film (9703, 3M, 50 µm, ACF) was laser cut into the same size as the fabricated AgNW-PUA unit and then transferred onto the AgNW-PUA unit to form the base electrode. Next, the ACF top surface was covered with a mask, which was made by laser-patterning of the ACF's original liner. A 200 nm-thick gold (Au) layer was deposited onto the ACF/AgNW/PUA electrode via e-beam evaporation. All electrochemical methods were performed by a potentiostat (CHI E660). To construct platinum (Pt)-SIBs for electrochemical staining and sensing experiments, platinum nanoparticles (PtNP) were deposited onto the Au/AgNW/PUA electrodes via chemical reduction in an aqueous solution of 2.5 mM H<sub>2</sub>PtCl<sub>6</sub> (Sigma-Aldrich) and 1.5 mM formic acid (Sigma-Aldrich) at -0.1 V (vs. Ag/AgCl) for 10 min. To construct iridium oxide (IrOx)-SIB, IrOx was electrodeposited on Pt/Au/ACF/AgNW/PUA by cyclic voltammetry (CV, 0 - 0.6 V vs. Ag/AgCl, 50 mV/s, 100 cycles) in the prepared aqueous solution. The solution contains 4.5 mM iridium tetrachloride (Sigma-Aldrich), 1% (v/v) hydrogen peroxide (30% wt., Sigma-Aldrich) and 55.5 mM oxalic acid dihydrate (Sigma-Aldrich) with a pH of 10.5, titrated by potassium carbonate (Sigma-Aldrich). The obtained solution was allowed to stabilize for at least 48 h before use. The properties of IrOx-SIBs are compared with commercialized cuff electrodes (MicroProbes Inc.). For carbon-SIB fabrication, the ACF/AgNW/PUA electrode with a laserpatterned liner was first affixed to a glass substrate for spin coating. A small amount of carbon ink (Ercon, E3449) was transferred onto the top ACF surface and spin coated at 4000 rpm, 60s. Then the electrode was baked at 60 °C for 10 mins.

### Electrical characterization of SIBs

Samples were fixed onto a linear motion stage. A multimeter was used to directly probe the silver nanowire contact pad to obtain the resistance value of samples. Sheet resistance was calculated based on the measured length and estimated width of samples (assume Poisson's ratio = 0.2) under different strain conditions.

## Electrochemical characterization of SIBs under different strain conditions

A linear motion stage was used to apply the desired strain levels to the SIBs. For static tensile strain studies, the SIBs' tensile strain states were preserved with the aid of a customized rigid frame, before transferring them from the stage into a beaker for electrochemical characterization. In this setting, Ag/AgCl and Pt were used as the reference and counter electrodes. Paired t-test was used to investigate statistical significance of sensing/CV results (with only one variable) and the two sample K-S test was used to investigate statistical significance of EIS curves across measurement groups. For dynamic tensile strain studies, electrochemical characterizations were performed with the SIBs affixed to the linear motion (applying dynamic strain levels), while

ensuring the preservation of the fluidic connection with an Ag/AgCl electrode. The performed electrochemical characterization methods are detailed below:

EIS characterization: the impedance spectrum of Au- and IrOx-SIBs (w/ and w/o strain) were measured by applying a 10 mV-amplitude sine wave at different frequencies (1 - 10<sup>5</sup> Hz) in a beaker containing a phosphate-buffered saline (PBS) solution.

CV characterization: for Au-SIBs (w/ and w/o strain), current signals were recorded by sweeping the voltage from -0.1 V and 0.5 V in 0.1 M KCl solution containing 5.0 mM  $K_3$ Fe(CN)<sub>6</sub> with scan rate of 50 mV/s. For Pt-, carbon-, and IrOx-SIBs, current signals were recorded by sweeping the voltage from -0.3 V and 1.4 V in 0.1 M  $H_2$ SO<sub>4</sub> solution at the scan rate of 100 mV/s.

Amperometry characterization: to characterize the H<sub>2</sub>O<sub>2</sub> sensing capability of Pt-SIBs (w/ and w/o strain), amperometric measurements were performed at +0.3 V. Responses were continuously recorded by a potentiostat under constant sample stirring. The calibration plots were constructed by spiking the sample (PBS) with different concentrations of H<sub>2</sub>O<sub>2</sub>.

Differential pulse voltammetry (DPV): to characterize the acetaminophen (APAP) sensing capability of carbon-SIBs (w/ and w/o strain), DPV measurements were performed in a beaker system. Voltage was scanned from +0.2 V to +0.8 V (increments: 5 mV, amplitude: 50 mV, pulse width: 0.05 s, sampling width: 16.7 ms, pulse period: 0.5 s).

Potentiometry (open circuit potential): to characterize the pH sensing capability of IrOx-SIBs (w/ and w/o strain), OCP measurements were performed using pre-titrated droplets (prepared via introducing NaOH/HCl into PBS), with pH levels spanning from ~ 6.5 to 8.

Biphasic potential pulses stimulation: to characterize the ex-vivo nerve stimulation capability of IrOx-SIBs (w/ and w/o strain), a series of +0.5 V to -0.5 V biphasic potential pulses (f = 25 Hz) were continuously applied to the IrOx-SIBs. The current was continuously recorded, while the IrOx-SIBs were immersed in the PBS solution.

Charge storage capacity (CSC) characterization: the CSC of the IrOx-SIB and ACF/AgNW/PUA electrodes were characterized by performing cyclic voltammetry (0.6 V to +0.8 V, at 50 mV/scan rate) in a 0.1 M KCl solution.

### In-vitro biocompatibility test

The cell toxicity was evaluated based on the mouse embryonic fibroblasts system (MEFs). MEFs were isolated from female embryos using a Pierce<sup>TM</sup> Mouse Embryonic Fibroblast Isolation Kit (Fisher, #88290), from pregnant female C57BL/6 mice with no genetic modifications. Asfabricated devices or components were sterilized (UV for 15 mins) before being incubated in the medium (Dulbecco's Modified Eagle Medium) for 10 days under 37 °C (CO<sub>2</sub> incubator). The positive control group was designed by the addition of AgNO<sub>3</sub> (Sigma-Aldrich) into the medium to reach a concentration of 10 μg/mL. After the devices or components were removed from the medium, the MEFs were cultured in the conditioned medium added with 10% fetal bovine serum for 24 hours. To quantify the viability, the cells were resuspended in Trypan blue stain, loaded into

a hemocytometer, and counted manually under a microscope. Each study involved two biological replicates and two technical replicates.

## In-vivo sciatic nerve stimulation

Animal: six mixed gender, body weight 20-28g, 3-4-month-old C57BL/6J (C57BL/6J, Catalog No: 000664, The Jackson laboratory, ME USA 04609) mice were used in this study. All animal studies were performed according to the protocols approved by the University of California, Los Angeles Animal Research Committee, under the ARC protocol number 2019-019. The experimental sample size (5 mice in total) was determined by the similar study. The methods were carried out in accordance with the relevant guidelines and regulations in full compliance with the ARRIVE (Animal Research: Reporting of in vivo Experiments) guidelines 2.0.

Sciatic nerve stimulation: before each study, animals were weighed to make sure that their body weights were over 20 grams. Mice were anaesthetized by isoflurane via inhalation. The induction of the anesthesia was done with 3-5% isoflurane no longer than 2 min and the maintenance of the anesthesia was done with 0.5 - 2% isoflurane. Toe pinch was used to validate the state of anesthesia every 15 min throughout the entire procedure. The animals were placed on its side and the other hindlimb was put on a small cotton ball with adhesive tapes to keep the hindlimb stable. We found the femur using the forefinger and made an incision of approximately 0.5 cm, parallel to the femur and approximately 1.5 mm anterior to the femur. The muscles close to the femur were separated with a pair of blunt-tip forceps without cutting the muscles or nerves. The muscle layers could be separated easily without any bleeding and the sciatic nerve was then visible. In case of bleeding, we used a cotton-tipped swab to absorb the blood. Once the sciatic nerve was exposed, the IrOx-SIB was gently placed underneath across the main branch of the sciatic nerve to deliver the electrical stimulation. 5s-electrical stimulation pulses (pulse width: 10 ms, at least 5 repeats for each stimulation, resting period between stimulations: 1 min) were delivered to the sciatic nerve with either varying intensity or frequency in a randomized sequence. For stimulation data, it describes both technical replicates and biological replicates.

Electromyography (EMG) recording: the EMG recording was used to monitor and evaluate the muscle activities in response to the sciatic nerve stimulation. For this purpose, tibialis anterior (TA) and medial gastrocnemius (MG) muscles of anesthetized mice were exposed for EMG recording. The recording electrode wires were inserted to the muscles using a 27g needle, while the ground electrodes were placed on the ear of the animals. EMG signals were recorded throughout each stimulation or sham session with three phases of testing 1) pre-stimulation baseline (3 minutes), 2) sham or stimulation (5s), and 3) post-stimulation baseline (6 minutes). After the procedure, the animal was euthanized through 4% paraformaldehyde transcardiac perfusion.

Tissue processing and immunofluorescence staining: spinal cord tissues of the euthanized animal were sectioned coronally on a Leica CM1900 cryostat at 30 μm. All tissue slices were processed by 10% normal donkey serum for an hour at room temperature. The spinal cord was also stained for antibodies against c-Fos (ab190289, Abcam, RRID: AB\_2737414), CaMKII (MAB8699, Millipore, Millipore, RRID: AB\_2067919), and pCREB(sc-7978, Santa Cruz, RRID: AB\_2086020). Fluorescent conjugated secondary antibodies (488 anti-mouse, Catalog No: 715-547-003), Cy3 anti-rabbit (Catalog No: 711-165-152), Jackson Laboratory, Bar Harbor, ME) were

incubated with the tissue at room temperature for two hours in place of the aforementioned biotinylated secondary antibodies. After washing with PBS/T (Triton), the slides were mounted in Vector DAPI (Catalog No: H-1200) mounting solution (Vector Labs, Burlingame, CA) and examined using fluorescence microscopy (Echo Revolve).

## **Supplementary Text**

Text S1. Derivation of probability that a cracked fragment in the interfacial layer remains electrically connected via at least one conductive element in the ACF layer

To set up the problem, we denote a representative cracked fragment area as a, the total interfacial area as A, and the density of conductive elements within ACF as m. Following a simple binomial distribution and a conservative assumption that the surface area of the conductive elements can be neglected, the probability P that the cracked fragment in the interfacial layer overlaps with at least one underlying conductive element can be expressed as:

$$P = 1 - (1 - \frac{a}{A})^{ma}$$

In our context, A is 4 mm<sup>2</sup> and m is on average 106 particles per mm<sup>2</sup>. Thus, the probably that the cracked fragment remains electrically connected can be calculated as:

$$P = 1 - (1 - \frac{a}{A})^{424}$$

We utilized this probability expression to set the threshold for determining the electrical connection status of the fragments (here, 95%). By empirically characterizing the cracked fragments' sizes formed under different strain conditions (20%, 40%, and 80%) via SEM imaging, and applying the set threshold, we estimated the percentage of cumulative connected cracked fragments with respect to the original (uncracked) interfacial area (fig. S5B).

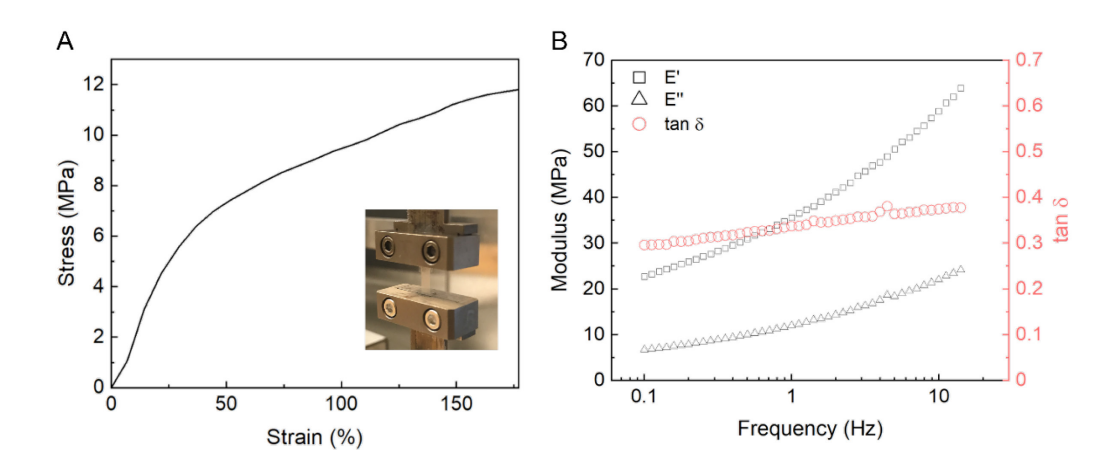


**Fig. S1. Mechanical characterizations of the ACF/AgNW/PUA composite.** (A) Uniaxial stress-strain curve of the ACF/AgNW/PUA. The ACF/AgNW/PUA can be stretched over 150%. Inset shows the tested device under tension. (B) Dynamic modulus characteristic of the composite.

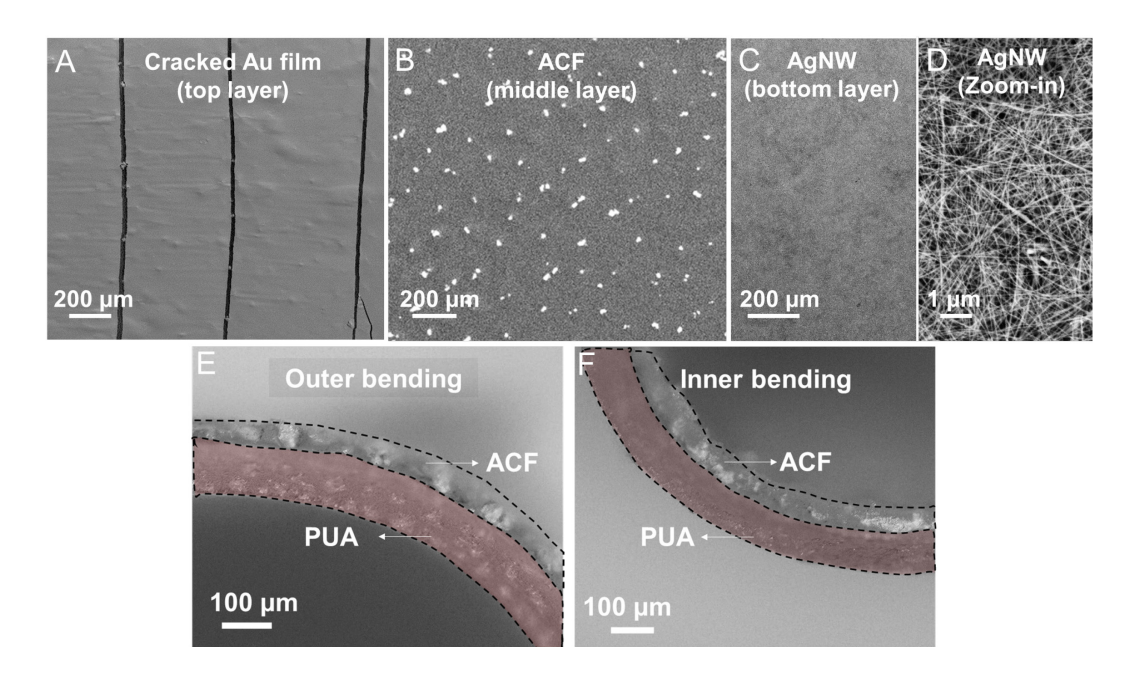


**Fig. S2.** Microscopic images of strain-accommodating features of SIB within each layer. SEM images of (A) cracked fragments under strain (top layer; interfacial material: Au), (B) embedded conductive elements within ACF (middle layer), and (C) AgNW network (bottom layer). (D) Zoom-in view of the AgNW layer illustrating submicron features. (E, F) Cross-sectional optical microscopic images of SIB illustrating the ACF and PUA layers under outer (E) and inner bending (F).

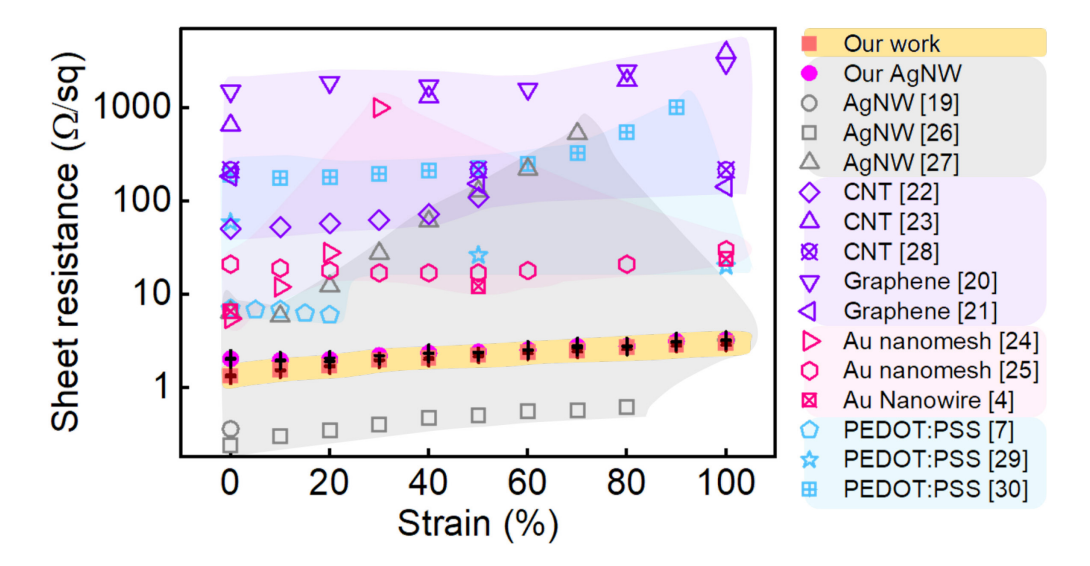


**Fig. S3. Sheet resistance under strain.** Comparison of the sheet resistance of the devised SIB (here, Au as the interfacial layer) and standalone AgNW/PUA vs. other stretchable conductors/electrodes, over the strain range of 0 to 100% (N = 3; error bars indicate SEM).

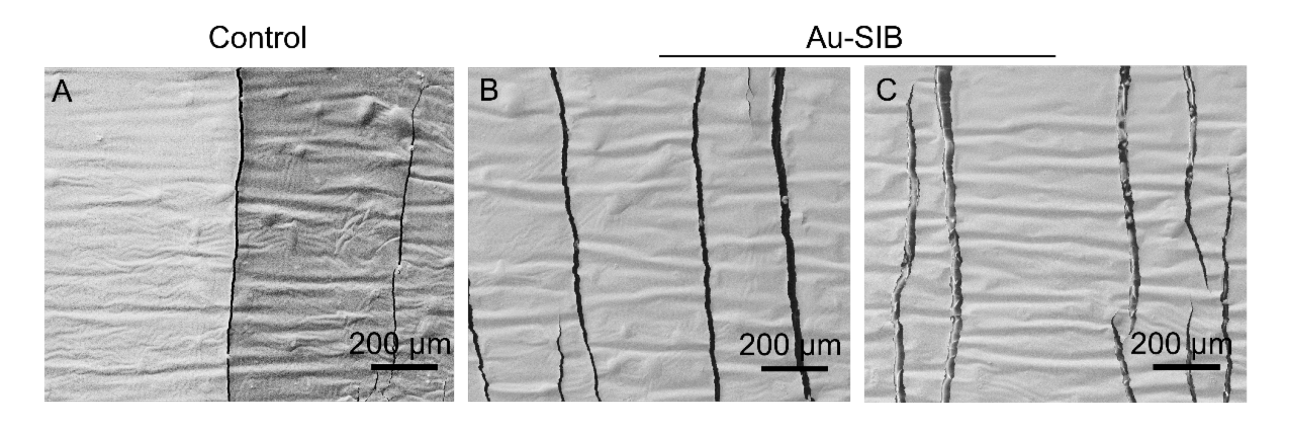


**Fig. S4. SEM images of electrochemically-stained electrodes under strain (A-C)** Corresponding original SEM images of the electrochemically-stained electrodes illustrated in Fig. 2.

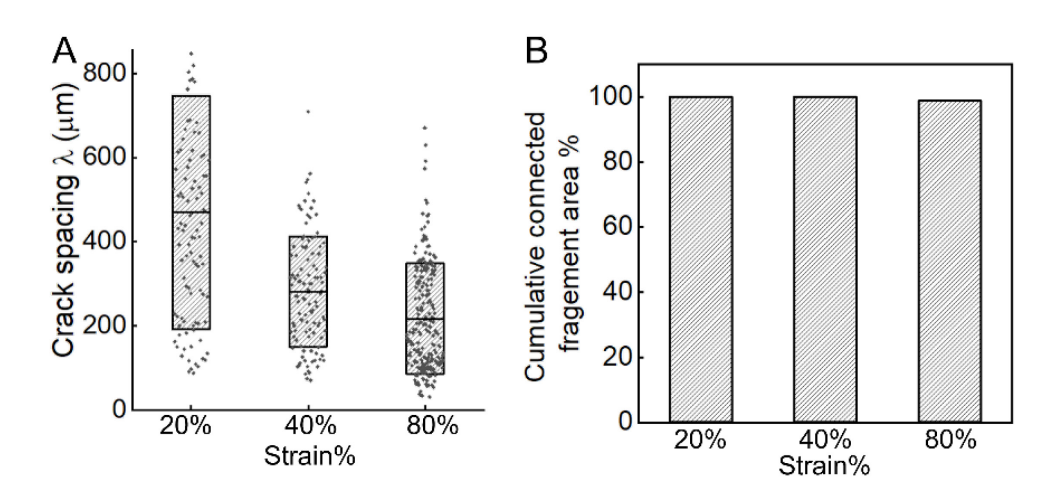


Fig. S5. SIB's cracked fragment size distribution under strain. (A) Characterization of the crack spacing of the SIB's interfacial layer (here, Au) at 20%, 40% and 80% strains using SEM imaging. The results indicate that the great majority of the cracked fragments' sizes are  $> 100 \, \mu m$  across all strains. (B) Estimated percentage of cumulative connected cracked fragments with respect to the original (uncracked) interfacial area (based on the analyzed SEM images of the cracked fragments' area and the statistical model described in Text S1).

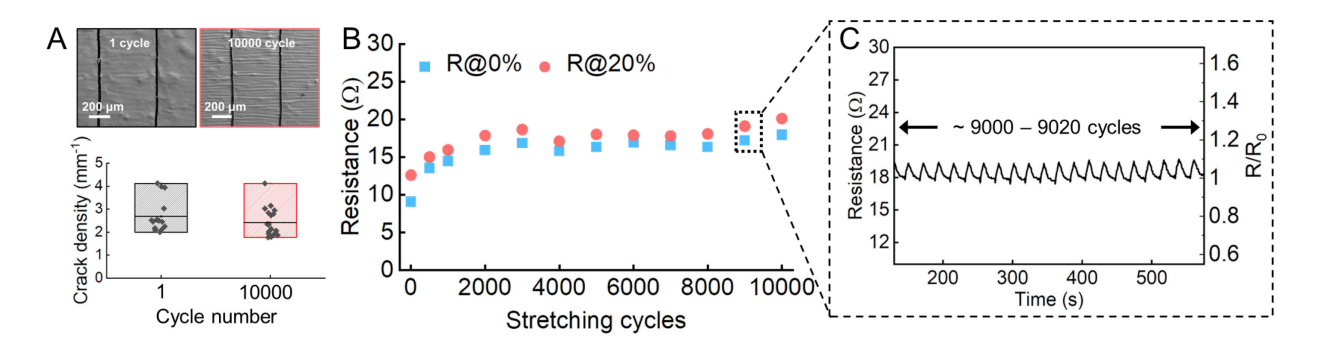


Fig. S6. SIB durability under cyclic stretching. (A) Characterization of the crack density of SIB's interfacial layer (here, Au) after 1 and 10,000 cycle(s) using SEM imaging (strain: 20%). Representative images of the formed cracks are shown atop. (B) SIB's resistance (red: at 20% strain; blue: at 0% strain) as a function of stretching cycles (test device: Au-SIB; strain: 20%; stretching rate: 12 mm/min). (C) Zoom-in view of real-time device resistance measurements within the time period in between the  $\sim$  9000th and 9020th cycles. The measurements indicate minimal change in device resistance ( $\sim$ 2  $\Omega$ ) under dynamic stretching strain.

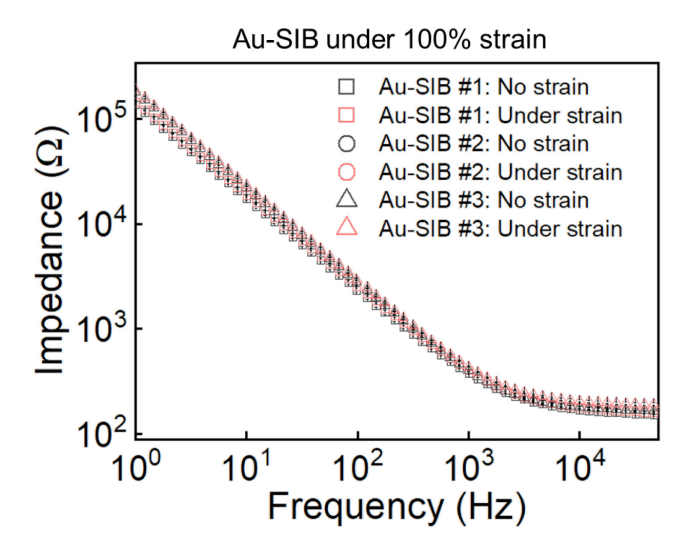
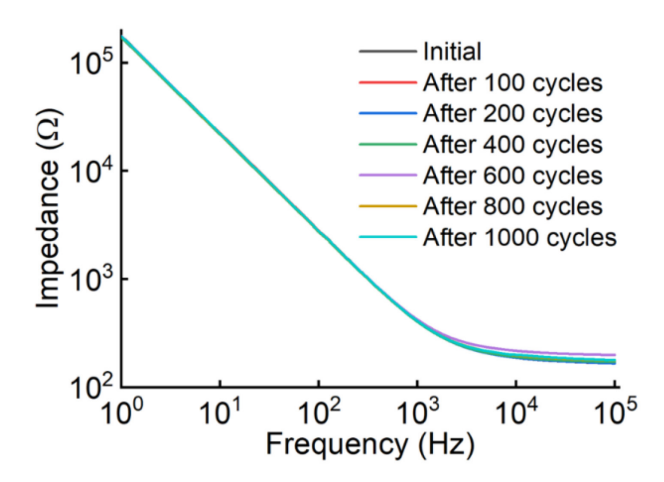


Fig. S7. Evaluation of EIS strain-insensitivity across different Au-SIBs. EIS measurements of three devices illustrate their strain insensitive performance. The p values comparing unrestrained vs. strained measurements for all devices are within the range of 0.12 - 0.98 (strain: 100%). Error bars indicate SEM. N = 3.



**Fig. S8. EIS characterization of Au-SIB under mechanical cycling test.** Initial and corresponding impedance spectrum of Au-SIB after 100, 200, 400, 800, and 1000 cycles of 10% uniaxial tensile strain, illustrating minimal impedance magnitude variation (< 8%, across the tested frequency range, after 1000 cycles).

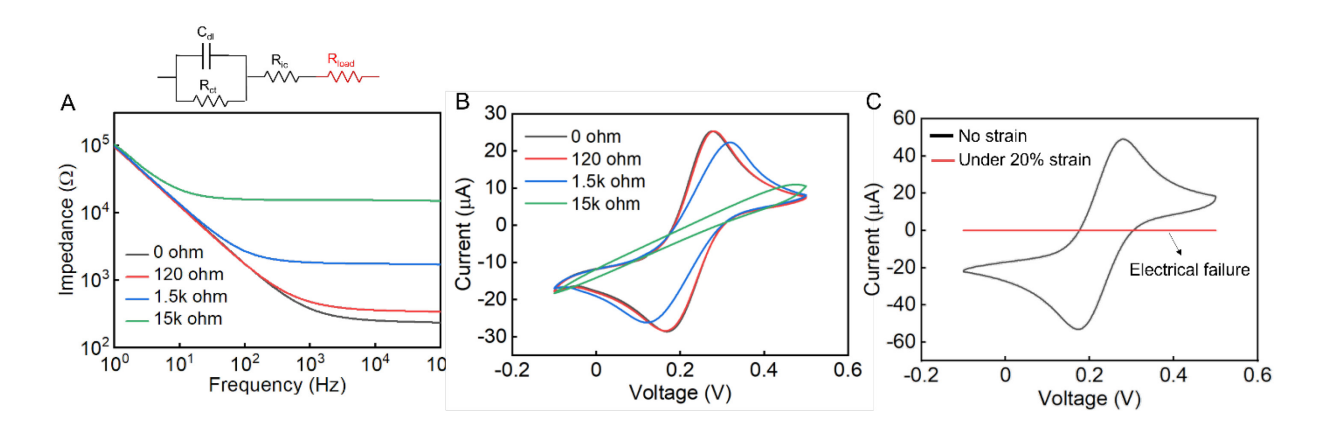
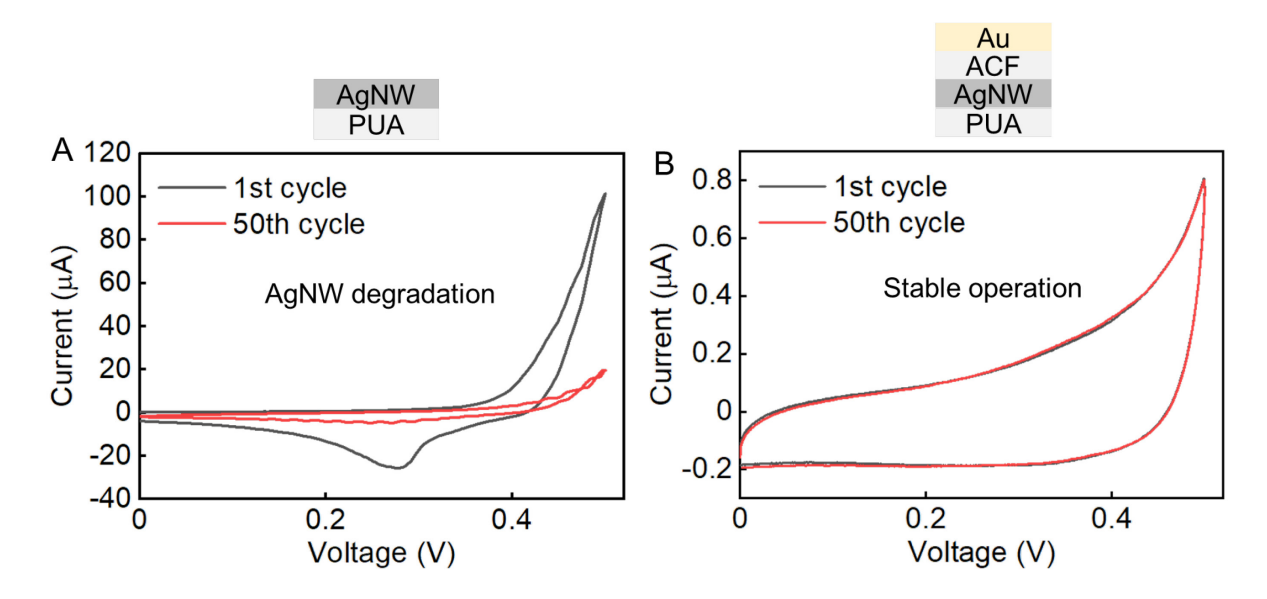


Fig. S9. Effect of the interconnect resistance (R<sub>ic</sub>) increase on the EIS and CV curves of non-strain resilient Au/PUA electrodes. (A) Impedance spectrum of a non-strain resilient model electrode (Au/PUA) with different interconnect resistances. R<sub>ic</sub> is changed by connecting different loading resistors (120, 1.5k, 15k ohm) in series with the interconnection trace. (B) CV profiles of the Au/PUA electrode with different interconnect resistances. (C) Comparison of the CV profile of the unstrained vs. under-strain Au/PUA, illustrating that the electrode becomes open circuit under the applied strain.



**Fig. S10. Electrochemical stability of electrodes**. CV plots corresponding to the 1st and 50th cycle of voltammetry (0.1 M Na<sub>2</sub>SO<sub>4</sub> aqueous solution), performed with a bare AgNW/PUA electrode (A) and Au-SIB (B).

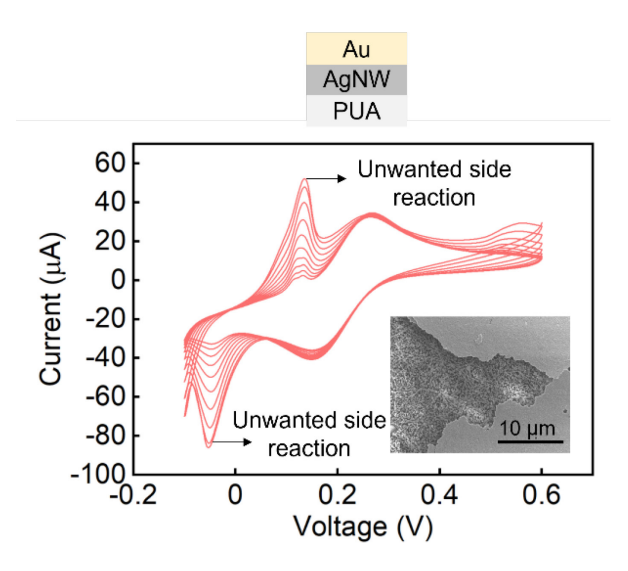


Fig. S11. Progressive CV characterization of Au/AgNW/PUA electrode (post-strained). The marked peaks are indicative of the unwanted silver oxidation and reduction processes, which occur due to the crack-induced exposure of the AgNWs to the electrolyte. The inset SEM figure shows the cracked Au-film and the exposed AgNWs (oxidized) underneath.

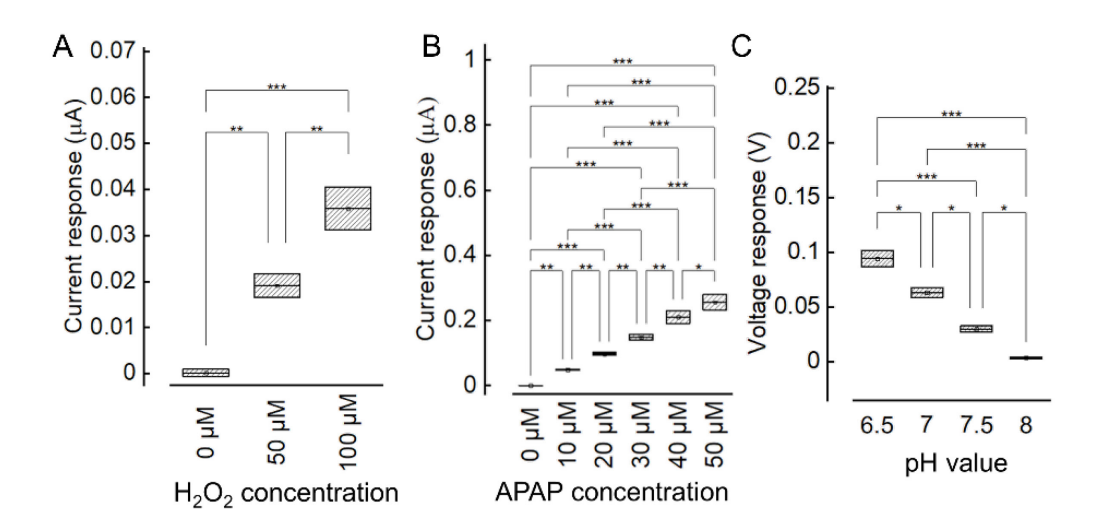


Fig. S12. Evaluation of device-to-device electrochemical performance variation. (A) Pt-SIB's responses to 0, 50, 100  $\mu$ M H<sub>2</sub>O<sub>2</sub> concentration. (B) Carbon-SIB's responses to 0-50  $\mu$ M APAP concentration. (C) IrOx-SIB's responses to pH conditions from 6.5 to 8. N = 3 across all measurements and error bars indicate SEM.

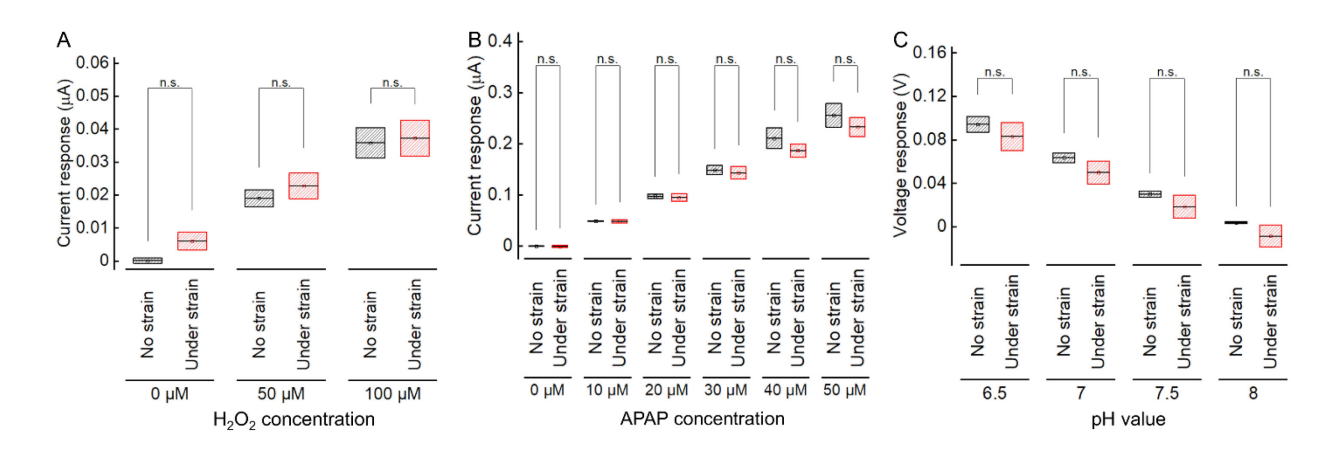


Fig. S13. Repeatability of SIB's strain-insensitive electrochemical performance. (A) Pt-SIB's  $H_2O_2$  responses (0, 50, 100  $\mu$ M) at 40% tensile strain vs. unstrained. (B) Carbon-SIB's APAP responses at 100% tensile strain vs. unstrained. (C) IrOx-SIB's pH OCP responses at 40% tensile strain vs. unstrained. N = 3 across all measurements and error bars indicate SEM.

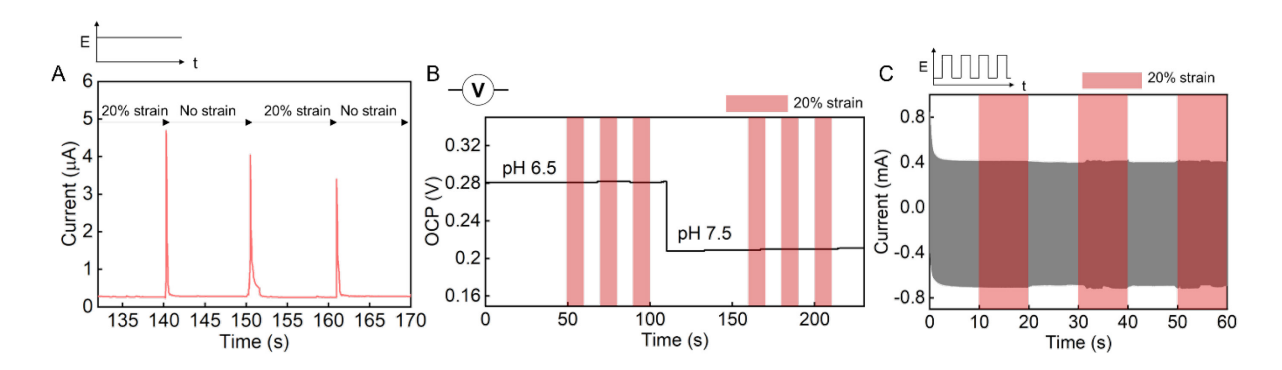


Fig. S14. Electrochemical sensing responses of Pt- and IrOx-SIBs under dynamic tensile strain. (A) Amperometric current profiles of a Pt-SIB in PBS solution under 20% dynamic tensile strain. It illustrates that the intermittently established steady-state baseline current stays the same, despite inevitable transient double layer capacitance discharging (I<sub>NF</sub> in Fig. 3C (ii)), which manifests as a current pulse (during stress loading/unloading). (B) Temporal pH responses of an IrOx-SIB under 20% dynamic tensile strain. (C) Ex-vivo stimulation current profile of an IrOx-SIB under 20% dynamic tensile strain (upon application of biphasic voltage pulses).

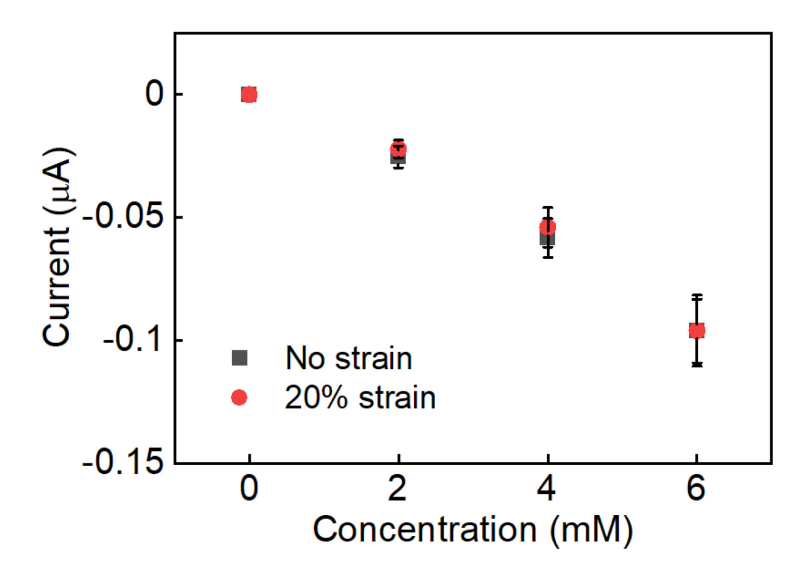
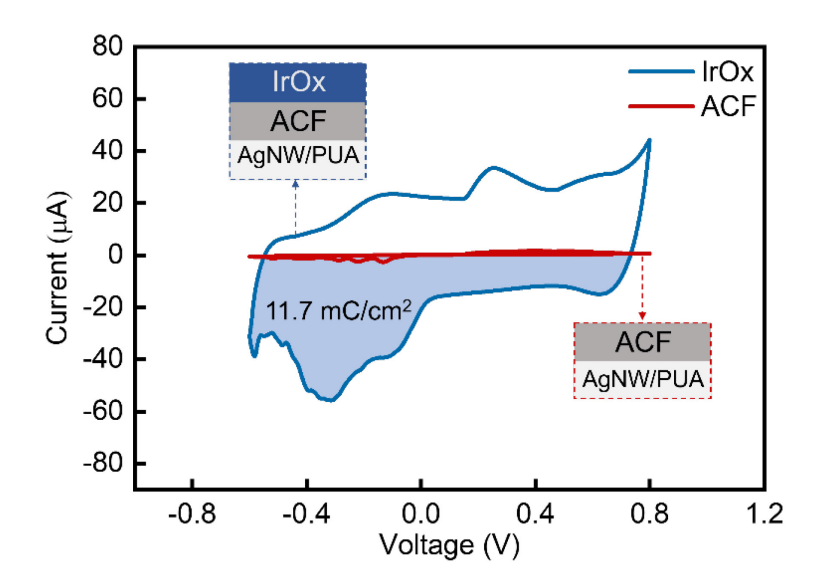


Fig. S15. Strain-insensitive  $H_2O_2$ -sensing using Au as an interfacial material. Comparison of device responses to  $H_2O_2$  (0 - 6 mM; -0.25 V) at 20% tensile strain vs. unstrained. N = 6 across all measurements and error bars indicate SEM.



**Fig. S16. CSC characterization of IrOx-SIB and ACF/AgNW/PUA electrodes.** CV profiles of an IrOx-SIB and a bare ACF/AgNW/PUA, illustrating the IrOx-SIB's high CSC (11.7 mC/cm²) and the electrochemical inertness of the bare ACF/AgNW/PUA electrode.

## IrOx under 40% strain IrOx-SIB #1: No strain IrOx-SIB #1:Under strain 10<sup>4</sup> IrOx-SIB #2:No strain Impedance $(\Omega)$ IrOx-SIB #2:Under strain IrOx-SIB #3:No strain IrOx-SIB #3:Under strain 10<sup>3</sup> 10<sup>2</sup> 10<sup>4</sup> 10<sup>0</sup> 10<sup>1</sup> 10<sup>2</sup> 10<sup>3</sup> Frequency (Hz)

Fig. S17. Evaluation of EIS strain-insensitivity across different IrOx-SIBs. EIS measurements of three devices illustrate their strain insensitive performance. The p values comparing unrestrained vs. strained measurements for all devices are within the range of 0.50 - 0.99 (strain: 40%). Error bars indicate SEM. N = 3.

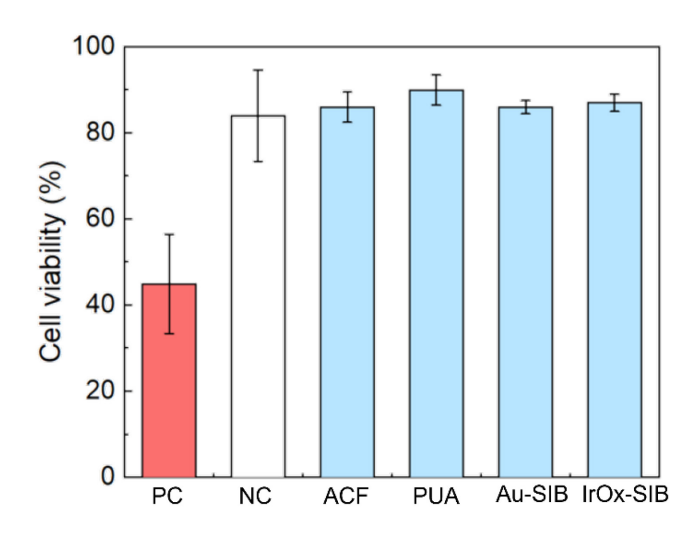


**Fig. S18.** Ex-vivo biocompatibility test. The results of cellular viability test. The cell toxicity was evaluated based on the mouse embryonic fibroblasts system. NC: negative control (blank). PC: positive control (Ag ion-spiked). Error bars indicate SD.

Table S1. Comparison with the state-of-the-art stretchable conductors and bioelectrodes.

		SIB (this work)	AgNW (5, 26)	Graphene (20, 21)	CNT (22, 23)	Nanomesh (24, 25)	Vertically- aligned AuNW (4, 6)
Electrochemical domain Electrical domain	Sheet resistance $(\Omega/\text{sq})$	Low (1.33)	Low (0.36)	High (10 <sup>2</sup> - 10 <sup>3</sup> )	High 10 <sup>1</sup> - 10 <sup>2</sup> )	Low (<10 <sup>1</sup> )	Low (<10 <sup>1</sup> )
	Sheet resistance at 100% strain (Ω/sq)	Low (2.98)	Low (3.24)	High (10 <sup>2</sup> - 10 <sup>3</sup> )	High (10³)	Open circuit at 30% strain	Relatively high (10¹)
	Withstand cyclic loading	Yes (>10 <sup>4</sup> cycles)	Yes (>10 <sup>3</sup> cycles)	Yes (>10 <sup>3</sup> cycles)	Yes (>10 <sup>3</sup> cycles)	Yes (>10 <sup>3</sup> cycles)	Yes (>10 <sup>4</sup> cycles)
	Electrochemical strain sensitivity $(\Delta Z/Z_0$ at 1 kHz)	Insensitive	N/A (corrosion limited)	Sensitive	Sensitive	Relatively sensitive	Not reported
	Electrochemical stability	High	Low	High	High	High	High
	Electrochemical functionality (stimulation/biomarker sensing)	Generalizable	Corrosion limited	Inefficient for stimulation	Inefficient for stimulation	Not demonstrated	Strain sensitive sensing